Slab Graph Convolutional Neural Network for Discovery of N_2 Electroreduction Catalysts

Myungjoon Kim[+], Byung Chul Yeo[+], Sang Soo Han[*], Donghun Kim[*]

Computational Science Research Center, Korea Institute of Science and Technology, Seoul 02792, Republic of Korea

[*]Correspondence to: donghun@kist.re.kr (D.K.); sangsoo@kist.re.kr (S.S.H.)
[+]Equal contributions

Abstract

The catalyst development for N_2 electroreduction reaction (NRR) with low onset potential and high Faradaic efficiency is highly desired, but remains challenging. Machine learning (ML) recently emerged as a complementary tool to accelerate material discovery; however a ML model for NRR has yet to be developed. Here, we develop and report slab-graph convolutional neural network (SGCNN), an accurate and flexible ML model that is applicable to catalytic surface reactions. With the self-accumulated database of 2,699 surface calculations, SGCNN predict binding energies, ranging over 8 eV, of five key adsorbates ($^*H$, $^*N_2$, $^*N_2H$, $^*NH$, $^*NH_2$) related to NRR performance with the mean-absolute-error of only 0.23eV. Unlike previously available models, SGCNN avoids using *ab initio* level inputs, instead is solely based on elemental properties that are all readily available in Periodic-Table-of-Elements; true accelerations can be realized. *t*-distributed stochastic neighbor embedding (*t*-SNE) analysis reveals that binary intermetallics of averaged *d*-electron occupation between 4 and 5 could potentially lower the onset potential in N_2 electroreduction.

Introduction

Copious amounts of ammonia (NH_3), the major component of fertilizer, are produced globally (>145 million tons/year).[1] Today, NH_3 production heavily relies on the energy-intensive and methane-based Haber-Bosch process (HBP). HBP must be operated under very harsh conditions (pressure 150-200 atm; temperature 300-500 ^oC)[2,3] using pure hydrogens that are mostly sourced from natural gas via steam reforming. As a result, ammonia productions today significantly contribute to greenhouse gas emission and climate changes. As an alternative to conventional HBP, an electrochemical reduction of N_2 to NH_3 has recently been pursued, as it offers more energy-efficient and eco-friendly (no CO_2 emission) routes.[4-8]

Tremendous efforts are recently put on developing catalysts that can electrochemically reduce N_2 to NH_3. A variety of catalysts are reported, such as Ru,[9,10] Fe,[5] Fe_2O_3,[11,12] Au,[13-15] N-doped carbon[16,17] but the production rates are far from satisfactory (orders of tens of $ug_{NH3}/mg^{-1}_{cat}\ h^{-1}$). In addition, Faradaic efficiencies of these catalysts are typically below 10% (low NH_3 selectivity), due to competing hydrogen evolution reactions. The development of more efficient and selective catalysts for N_2 electroreduction is highly desired, but remains slow and challenging.

Examining the potential catalyst-material space via high-throughput experiments and/or first-principles calculations is too time-consuming, and thus practically impossible. To overcome this limitation, machine learning (ML) has recently emerged as a powerful and complementary tool to potentially accelerate new material discovery.[18-27] ML models are developed to disentangle the complex catalyst-adsorbate interactions for various reactions including syngas reaction,[27] C-C cross-coupling reaction,[21] and CO_2 reduction,[18-20,22-24] and NO decomposition[26]; a model for N_2 elecroreduction has yet to be developed. In addition, the utility of these models for screening process still remains a challenge. Many models have *ab initio* level (*eg.* density-functional-theory (DFT)) surface features, such as *d*-band characteristics as key inputs, which requires additional DFT calculations for ML input preparations; true accelerations could not be realized. The development of ML models with lower

level inputs (*eg.* structure information or readily available property) is desirable for the catalyst screening purpose.

Graph-based convolutional neural network (GCNN) is our adoption, as graph representation can flexibly encode the structural information of materials. In GCNN scheme, material structures are represented as graphs whose vertices and edges correspond to atoms and bonds. Indeed, the graph representation combined with machine learning was successfully applied to molecular systems[28,29] and bulk solids[30-32]; however its application to surface-adsorbate systems is nonexistent yet, in which catalytic reactions are typically modeled. In this article, we first report slab-GCNN (SGCNN) model that is applicable to surface catalytic reactions. Our SGCNN model completely avoids using any *ab-initio* level input features, instead is fully based on the simplest inputs that are all readily available elemental properties in the Periodic-Table-of-Elements. With our own database of 2,699 surface DFT calculations, SGCNN predicts the binding energies of five adsorbates (H, N_2, N_2H, NH, NH_2) within mean-absolute-error (MAE) of 0.23 eV, which are directly related to N_2 electroreduction performances. *t*-distributed stochastic neighbor embedding (*t*-SNE) analysis suggests that binary intermetallics of averaged *d*-electron occupation between 4 and 5 could potentially lower the onset potential in N_2 electroreduction.

Results and Discussion

The present work focuses on two catalytic properties in N_2 electroreduction reactions: (1) limiting potential (or onset potential), and (2) Faradaic efficiency (or selectivity). To begin with the limiting potential, some recent studies on N_2 electroreductions over various pure metals suggest that one of the following two protonation steps governs the limiting potentials[33-34]: $^*N_2+H^++e^-\rightarrow{}^*N_2H$ ($^*N_2\rightarrow{}^*N_2H$ hereafter) vs. $^*NH+H^++e^-\rightarrow{}^*NH_2$ ($^*NH\rightarrow{}^*NH_2$ hereafter). DFT-computed free-energy (ΔG) diagrams for associative N_2 reduction pathways on Ru(001) and Ti(001) are shown in Fig. 1a. These two surfaces are shown as an exemplary case for each $^*N_2\rightarrow{}^*N_2H$ and $^*NH\rightarrow{}^*NH_2$ potential limiting step (PDS). For each transition metal, the most stable surface is selected, and the energetics calculations along full reaction paths of other metal cases are available in Fig. S1 of Supporting Information. All these calculations indicate that PDS is at $^*N_2\rightarrow{}^*N_2H$ for most of *late* transition metals (group numbers

7-11, *eg*. Fe, Ru, Rh, Ni, Pd) whereas PDS is at $^*NH \rightarrow {}^*NH_2$ for most of *early* transition metals (group numbers 3-5, *eg.* Sc, Ti) is at $^*NH \rightarrow {}^*NH_2$, which also agrees with literatures.[33-34]

The minimum applied voltage to make N_2 electroreduction pathway exergonic in all steps is defined as limiting potential (U_L). The energetics presented in Fig. 1b assume that PDS is either at $^*N_2 \rightarrow {}^*N_2H$ or $^*NH \rightarrow {}^*NH_2$, and U_L is defined as the maximum value of ($\Delta G_{N_2H} - \Delta G_{N_2}$) and ($\Delta G_{NH_2} - \Delta G_{NH}$). U_L of 24 metal surfaces are added on the map in Fig. 1b, and a linear relation is observed. A strategy to break the linear relation has yet to be found. Out of 24 metal surfaces on Fig. 1b, Mo(110) exhibits the lowest U_L of 0.89 Volt, and the most others exhibit U_L over 1.0 Volt. We highlight the promising zone of U_L less than 0.89 Volt so that any materials positioned in the zone require smaller onset potential than Mo(110) does.

The other important property for N_2 electroreduction is Faradaic efficiency. Faradaic efficiencies of previously studied catalysts are very low (typically below 10%), and this is mainly due to the competition with hydrogen evolution reaction. In this view, the binding energy difference between $^*N_2$ and $^*H$, defined as $F=\Delta G_{N2}-\Delta G_H$, on catalyst surfaces can serve as a great descriptor for determining Faradaic efficiency. The more negative *F* is for a catalyst material, the higher Faradaic efficiency it may potentially exhibit. Fig. 1c compares DFT-computed ΔG_{N2} and ΔG_H of 24 transition metals. Here, we also define promising zone of *F* less than -0.49 eV (Mo(110) value). Note that a few elements including Ag(111) and Au(111) are better than Mo(110) in the selectivity criterion; however the U_L values for these elements are too high to be used for N_2 electroreduction. Mo(110) is more suitable material as a reference.

The previous analysis indicates that binding energies of five adsorbates ($^*H$, $^*N_2$, $^*N_2H$, $^*NH$, $^*NH_2$) are directly related to catalytic performances. We generated our own database of DFT binding energies for these five adsorbates (2,699 data), summarized in Fig. 2. Total 465 catalysts are modeled in slab geometry, which include 30 unary and 435 binary systems. Binary systems are either ordered intermetallics (OI) or core-shell (CS) type alloy that is composed of transition metal elements in periods 4-6 and groups 3-12 in Periodic-Table-of-Element (Fig. 2a and 2b). Of all possible elemental

combinations ($_{30}C_2$=870), nearly half are excluded for DFT computations. For OI, materials of bulk formation energy (E_f) less than 0.1 eV are selected for computations (172 systems), since thermodynamic mixing of elements would be difficult for E_f>0.1 eV cases. For CS, the strain of shell (ε) experiencing due to lattice mismatch with core element is considered, and materials of |ε|<5% (both tensile and compressive) are selected for computations (263 systems). See data preparation part of Methods for details.

For each catalyst material, five different adsorbates ($^*H$, $^*N_2$, $^*N_2H$, $^*NH$ and $^*NH_2$) are considered, since binding energies of these adsorbates are directly related to U_L or *F* determination (Fig. 2c). The interaction chemistry between catalyst surface and adsorbates substantially differ by adsorbate types. This is confirmed by the binding energy (E_{ads}) variations for each adsorbate. For $^*H$ or $^*N_2$ as examples, E_{ads} is relatively small, and ranges over only 2 eV. This is contrasted by the other three adsorbates cases ($^*N_2H$, $^*NH$ and $^*NH_2$) where E_{ads} is generally larger in magnitude and the variations are also large over 6 eV. We highlight that the database (2,699 data) is uniformly sampled over a wide range of chemical elements (30 elements), catalyst materials (OI and CS types), adsorbates (5 types) and binding energy (over 8 eV). Such wide and uniform sampling is critical for ML model training and tests.

With the database established, we now introduce a new ML model, namely, slab-graph convolutional neural network (SGCNN). SGCNN is an extended model of crystal-graph CNN (CGCNN) that is applicable to bulk solids, recently developed by Grossman and coworkers at MIT.[30] Although CGCNN has proven its excellence in predicting several bulk properties, such as bulk formation energy, band gap, and elastic constants etc., surface-related property cannot be tested because the graph structure is limited to bulk solids. Hence, its application to catalyst systems (mostly surface reactions) is not possible. Here, in order to solve this critical problem and to incorporate surface effects, we constructed two independent graphs. One is bulk graph (B), which is identical to the one in CGCNN model, and the other is surface graph (S_1 or S_2) that is based from adsorbates and top one (S_1) or two (S_2) surface layers. In each graph, nodes represent atoms and edges represent connections between atoms. The convolution layers and pooling layer were built on top of each bulk and surface graphs. Two pooled vectors originating from each bulk and surface graphs are

concatenated, which is finally related to adsorbate binding energy *via* fully-connected-network (FCN). All detailed information on graph constructions, neural network architecture (including convolution and pooling functions), hyperparameter tuning, regularization, and code availability are well elaborated in the Method section.

SGCNN performs very well in predicting adsorbate binding energies, as shown in Fig. 4a. For optimization, we tested total five graphs: B (bulk graph), S_1 (surface graph with top 1 layer), S_2 (surface graph with top 2 layers), $B+S_1$, and $B+S_2$. With no surprise, bulk only graph (B) performs very poorly as it does not incorporate surface effects at all. S_2 (or $B+S_2$) performs better than S_1 (or $B+S_1$), which may indicates that both top and sub-surface layer interacts with adsorbates. Out of five graphs, $B+S_2$ performs the best, leading to the mean-absolute-error (MAE) at 0.23 eV, estimated after 5-fold cross-validations. Previous ML models primarily developed for CO_2 reduction catalysis also report comparable digits of MAE or root-mean-squared-error (RMSE) around 0.12-0.3 eV for CO binding energy predictions. However, it should be importantly noted that binding energies in our database range over 8 eV, unlike previous works where CO binding energies range only about 2 eV. Further discussion on the level of accuracy is available in Table S2 of Supporting Information, with comparisons with other models in literature.

In Fig. 3d, we report results by catalyst types (OI vs. CS). Regardless of graph structures, adsorption energies for miscible alloy are relatively difficult for SGCNN to learn, compared to core-shell cases. For $B+S_2$ structure as an example, MAE of OI data is 0.34 eV and MAE of CS data is 0.14 eV. This is because, for CS data, adsorption energies are much dependent on shell element only (little dependence on core element), leading to the interaction chemistry relatively simpler. We also report the prediction accuracy by adsorbate types ($^*N_2$, $^*N_2H$, $^*NH$, $^*NH_2$) in Fig. 3e. The MAE variation is fairly small over all adsorbates (MAE 0.21 eV for $^*N_2$ and 0.29 eV for $^*NH$. Binding energy range of each adsorbate dataset (*eg*. 2 eV for $^*N_2$, and 6 eV for $^*NH$) relatively less affects the final MAE values, instead the fairly uniform MAEs were observed for all adsorbates. It should also be emphasized that SGCNN of a single weight-set can very well predict the binding energy data of multiple adsorbates.

The level of input features used for SGCNN training is critical for accelerated screening purpose. Some previous works have used DFT-computed surface features, such as *d*-band features (*d*-band centre or shapes) as key inputs.[22,24] These models well capture the catalyst-adsorbate interaction, likely owing to the strong correlation between *d*-band centre and adsorption energies. However, their usage for accelerated screening process remains a challenge, as they require additional DFT computations for input preparations. To overcome this critical problem, SGCNN is fully based on the simplest inputs that are all readily available from Periodic-Table-of-Elements. 12 elemental properties were considered (Fig. 4a), including group number (GR), period number (PR), electronegativity (EN), the 1st ionization energy (IE, in eV unit), electron affinity (EA, in eV unit), density (g/cm^3), atomic weight (AW, in g/mol unit), covalent radius (Å), atomic volume (AV, in cm^3/mol unit), melting point (℃), boiling point (℃), effective nuclear charge (Z_{eff}).[35]

A certain and partly combination of these features would lead to minimum prediction error, and we carried out a process to identify it. Exploring all possible combinations ($\sum_{n=1}^{12}{}_{12}C_n$) is too time-consuming, and thus the process was performed in a simpler way (Fig. 4b). Out of 12 features, the feature that gives the smallest error (in this case, group number) is first adopted, and keeps being added by another that reduces the error the most, and the process stops when the addition of any available feature no longer reduces the error. The best combinations leading to the minimum MAE of 0.23 eV constitute only five features, i.e., GR, EN, AV, EN, and AW. The additions of any feature to this combination increase the prediction accuracy due to overfitting (inset of Fig. 4b). It is notable that GR alone can lead to MAE of 0.28 eV, indicating its superior importance in predicting adsorption energies. GR of an element is linearly correlated with *d*-block electron number of the same; thus it may serve as an alternative descriptor of *d*-band centre of catalyst material.

The occlusion sensitivity test is performed to compare the importance/sensitivity of each atom or bond vector. Fig. 4c shows the increase of MAE (ΔMAE) when a specific feature of atom nodes either in bulk or surface graph is *occluded*, *i.e.*, nullified with all zero entries. The test reveals that atomic features of the surface graph are much more important than those of bulk graph. The occlusion of GR of surface graph leads to a severe malfunction of SGCNN with ΔMAE of 0.99 eV. The

occlusion test was also performed for bond vectors. Three types of bond vectors are occluded, including slab-slab, slab-adsorbate, and adsorbate-adsorbate. The SGCNN model is relatively less sensitive on bonds within slabs (ΔMAE=0.09 eV) or within adsorbates (ΔMAE=0.04 eV), compared to bonds between slab and adsorbate (ΔMAE=0.16 eV). This indicates that the proper descriptor of slab-adsorbate bonds (both the presence/absence of bond and its length) is critical to accurately predict adsorption energies.

t-SNE analysis[36] was performed to group promising catalyst materials. Since binding energies of four adsorbates ($^*N_2$, $^*N_2H$, $^*NH$ and $^*NH_2$) determines U_L, we first compute the pearson correlation (ρ_{corr}) between binding energy of each adsorbate and U_L, and identified that of $^*NH_2$ is the most strongly correlated with ρ_{corr}=0.73. The feature vectors of $^*NH_2$ are used for *t*-SNE analysis, and each site (representing each catalyst material) in Fig. 5b is coloured by U_L. The low U_L (<1.0 eV) vs. high U_L (>2.0 eV) regions are clearly grouped and distinguished in the space. The low U_L region mostly consists of OI type materials (●), rather than CS type (◆). This implies that binary OI compounds can break the known linear relations (line on Fig. 1b), whereas CS type materials are unlikely to do.

Another *t*-SNE analysis follows with each site coloured by d^*-4.5 where d^* is the averaged *d*-electron occupation of top surface layer (see the Fig. 5 caption for definition). *t*-SNE results in Fig. 5b and Fig. 5c show a large resemblance in the colour distribution, indicating that low U_L materials mostly exhibit d^* between 4 and 5. For binary OIs in the low U_L zone have one element as an *early* transition metal (group numbers 3-5; Sc, Y, Lu, Ti, Zr, Hf, V, Nb, Ta) and the other element as a *late* transition metal (group numbers 7-11; Mn, Tc, Re, Fe, Ru, Os, Co, Rh, Ir, Ni, Pd, Pt, Cu, Ag, Au). We emphasize that binary OI compounds is a great material space for discovering low UL material, and OI with d^* between 4 and 5 is particularly promising.

Conclusion

Overall, we have developed a machine-learning model SGCNN suited for NRR catalytic reactions. In this work, with self-accumulated database of 2,699 surface DFT

calculations, SGCNN predicts the binding energies of five adsorbates ($^*H$, $^*N_2$, $^*N_2H$, $^*NH$, $^*NH_2$), with MAE of only 0.23 eV, that are directly related to NRR catalytic performances. SGCNN avoids using *ab initio* level inputs, instead is merely based on elemental properties (GR, EN, AV, EN, and AW) that are all readily available in Periodic-Table-of-Elements. As a result, the model is suited for accelerated screening process. *t*-SNE analysis follows, and reveals that binary intermetallics of averaged *d* electron occupation (d^*) between 4 and 5 may substantially lower the onset potential in NRR.

Methods

DFT calculations for adsorption energy data accumulation. Spin-polarized DFT calculations were performed using Vienna ab initio simulation package (VASP) with projector-augmented-wave pseudopotentials[37,38] and RPBE (revised Perdew-Burke-Ernzerhof)[39]exchange-correlation functional. Grimme's DFT-D3 method was adopted to describe van der Waals interaction.[40] A plane-wave kinetic energy cutoff of 520 eV and the 6×6×1 Monkhorst-Pack *k*-point mesh was used.[41] For slab surface calculations, close-packed surfaces of each crystal structure are considered: (111) for fcc metals or $L1_0$ compounds, (001) for hcp metals, and (110) for bcc metals or B2 compounds. The slab of of 2×2 unitcell consists of 4 layers. The bottom two layers are fixed, and the top two layers and adsorbates are fully relaxed until the forces acting on the individual atoms are less than 0.05 eV $Å^{-1}$. 15 Å of vacuum spacing (in *z*-direction) was used to prevent spurious interactions between slabs. Various adsorbate positions on slabs are considered as follows: (1) H and N_2 adsorbates are placed vertically on the slab at top sites, (2) N_2H adsorbates are placed horizontally on the slab at top, hollow, and bridge sites, and (3) NH and NH_2 adsorbates are placed horizontally on the slab at top, hollow, and bridge sites. The detailed information is summarized in Figure S1. The adsorbate binding energies were calculated by the following equation: $\Delta E_{ads.}$ = E[slab+ads.] – E[slab] – E[ads.], where E[slab+ads.], E[slab], and E[ads.] are the total energy of slab+adsorbate, slab only, and adsorbate only. During SGCNN training, N_2H, NH, NH_2, E[ads.] was not referenced to N_2 or H_2 gas, but referenced to radical itself for enhanced prediction accuracy.

Free energy corrections. Free energies of adsorbates are estimated under standard reaction conditions (pH = 0, 298 K, 1 atm) at a potential of U = 0. The chemical

potential of ($H^+ + e^-$) is estimated equal to that of $0.5H_2$. The thermochemical free energy as given by $\Delta G_{ads.} = \Delta E_{ads.} + \Delta G_{corr}$, where $\Delta G_{ads.}$ and ΔG_{corr}. are free adsorption energy and free energy correction.[42] Importantly note that $\Delta E_{ads.}$ is referenced to N_2 and H_2 gas for $\Delta G_{ads.}$ estimations. ΔG_{corr} were estimated using a standard vibrational correction in the harmonic approximation to enthalpy and entropy, as follows: $\Delta G_{corr} = \Delta G_{ZPE} + \Delta H_{corr} - T\Delta S_{corr}$, where ΔG_{ZPE}, ΔH_{corr}, and $T\Delta S_{corr}$ are the zero-point energy correction, enthalpy correction, and entropy correction term. The detailed digits are summarized in Table S1. Solvation effects are ignored since the solvation-induced stabilization energy of adsorbates in the N_2 electroreduction is less than 0.1 eV.[43]

Slab graph constructions. Graphs are mathematical representations of system structures. Each graph consists of nodes and edges, which correspond to atoms and bonds, respectively. Note that multiple edges are allowed to represent periodicity of solids. The first step of building SGCNN is to construct two independent graphs: a bulk graph (B) and a surface graph (S_1 or S_2). The bulk graph (B) is identical to the one in CGCNN in the Xie and Grossman's approach (*4-3*). We propose the surface graph (S_1 or S_2) that is based from adsorbates and top one (S_1) or two (S_2) surface layers. The surface graph captures the catalyst-adsorbate interactions by characterizing adsorbate types, adsorption sites, and the bond lengths. All atoms (nodes) in the system are encoded into the atom vectors v_i. Each atom vector contains the periodic-table-level features. Atomic features are encoded as 'one-hot' manner due to its categorical property (not ordered). The used features are all readily available elemental properties from Periodic-Table-of-Elements. Bonds (edges) between atom *i* and *j* are defined only if $r_i + r_j > d_{(i,j)} + \Delta$, where $d_{(i,j)}$ is a distance between atom *i* and *j*, r_i, r_j denote radius of atoms, and the tolerance $\Delta = 1.5$Å. Bonds (edges) are encoded to bond vectors $u_{(i,j)_k}$ (*k* as the k^{th} edge connecting atom i and j) as follows[36]:

$u_{(i,j)_k}[n] = \exp(-(d_{(i,j)_k} - \mu_n)^2/\sigma^2$, where $\mu_n = n \cdot 2.4$ Å, $\sigma = 0.2$ Å.

CNN architecture. Convolutional neural network (CNN) are built on top of each bulk and surface graph. SGCNN consists of a sequence of convolutional layers (*t,f*), pooling layers, and fully-connected networks (FCN). First, the convolution functions first concatenate neighbor vectors $z_{(i,j)_k}^{(t,f)} = v_i^{(t,f)} \oplus v_j^{(t,f)} \oplus u_{(i,j)_k}$, and then convolute with *f* filters over *t* layers, as follows.

$$\mathrm{v}_i^{(t+1,f)} = v_i^{(t,f)} + \sum_{j,k} \sigma(z_{(i,j)_k}^{(t,f)} W_f^{(t,f)}, + b_f^{(t,f)}) \odot g\left(z_{(i,j)_k}^{(t,f)} W_s^{(t,f)} + b_s^{(t,f)}\right)$$

where $\oplus$ denotes concatenation, $\odot$ denotes element-wise multiplication, (t,f)=(number of convolution layer, number of convolution filters), σ is a sigmoid function and g is exponential linear units (ELUs) activation function.[44] Next, we select pooling function as the normalized summation of all atom vectors (after convolutions), i.e., $\mathrm{v}_{\mathrm{pool}} = \sum_i v_i^{(t,f)}$. As a result of pooling, the final feature vector is extracted in the same dimension with each atom vector. Two pooled vectors originating from each bulk and surface graphs are concatenated, which is finally related to adsorbate binding energy *via* fully-connected-network (FCN). The loss function $J(\mathrm{y}, \hat{y}(\boldsymbol{W}))$ is set as mean squared error (MSE). During training phase to minimize the loss function J using Adam optimization algorithm.[45]

Hyperparameter tuning and regularization. Following hyper-parameters are tested and the optimized values are shown in the parenthesis: the number of convolution filters and layers (1 filter 1, 3 layers), learning rate (5×10^{-3}), exponential decaying learning rate (0.97 for every 100 epoch), layers and nodes of FCN (3 layers with 10→2→1 nodes/layer), standard deviation of normal distributed random initial weights (0.1), batch size (64), and total number of epochs (1000). Two regularization techniques are used to reduce overfitting: dropout[46] and $\mathbf{L^2}$ weight decay. For dropout, we intentionally disconnect some neurons randomly during the training phase with a given probability. The optimized dropout probability and $\mathbf{L^2}$ regularization coefficients are 0.2 and 10^{-2}, respectively. A list of hyperparameters and their ranges for the optimization process are summarized in Fig. S3 and Table S3, S4 of Supporting Information.

SGCNN code availability. The proposed SGCNN is implemented in Python (version 3.5) using TensorFlow framework (version 1.7.0). Regarding the training time, it takes approximately an hour to obtain 5-fold cross-validation results per each SGCNN network using GeForce GTX 1080 Ti GPU. The SGCNN implementation code is available at https://github.com/myungjoon/SGCNN.

References

[1] U.S. Geological Survey, *Mineral Commodity Summaries* **2016**
[2] Smil, V. Enriching the earth: Fritz Haber, Carl Bosch, and the transformation of world food production; MIT Press: Cambridge, MA, **2004**
[3] Catalytic ammonia synthesis: fundamentals and practice; Jennings, J. R., Ed.; Springer Science & Business Media: New York, **2013**.
[4] Foster, S. L.; Perez Bakovic, S. I.; Duda, R. D.; Maheshwari, S.; Milton, R. D.; Minteer, S. D.; Janik, M. J.; Renner, J. N.; Greenlee, L. F. Catalysts for nitrogen reduction to ammonia. *Nat. Catal*. **2018**, 1, 490-500
[5] Renner, J. N.; Greenlee, L. F.; Ayres, K. E.; Herring, A. M. Electrochemical synthesis of ammonia: A low pressure, low temperature approach. *Electrochem. Soc. Interface* **2015**, 24, 51−57.
[6] Shipman, M. A.; Symes, M. D. Recent progress towards the electrosynthesis of ammonia from sustainable resources. *Catal. Today* **2017**, 286, 57−68.
[7] Kyriakou, V.; Garagounis, I.; Vasileiou, E.; Vourros, A.; Stoukides, M. Progress in the electrochemical synthesis of ammonia. *Catal. Today* **2017**, 286, 2−13.
[8] Guo, C.; Ran, J.; Vasileff, A.; Qiao, S. Z. Rational design of electrocatalysts and photo(electro)catalysts for nitrogen reduction to ammonia (NH_3) under ambient conditions. *Energy Environ. Sci*. **2018**, 11, 45−56.
[9] Kordali, V.; Kyriacou, G.; Lambrou, Ch. *Chem. Commun*. **2000**, 17, 1673
[10] Geng, Z.; Liu, Y.; Kong, X.; Li, P.; Li, K.; Liu, Z.; Du, J.; Shu, M.; Si, R.; Zeng, J. Achieving a record-high yield rate of 120.9 ugNH3 mg-1 h-1 for N2 electrochemical reduction over Ru single-atom catalysts. *Adv. Mater*. **2018**, 30, 1803498
[11] Licht, S.; Cui, B. C.; Wang, B. H.; Li, F.-F.; Lau, J.; Liu, S. Z. Ammonia synthesis by N_2 and steam electrolysis in molten hydroxide suspensions of nanoscle Fe_2O_3. *Science* **2014**, 345, 637-340
[12] Chen, S.; Perathoner, S.; Ampelli, C.; Mebrahtu, C.; Su, D.; Centi, G. *Angew. Chem. Int. Ed.* **2017**, 56, 2699
[13] Li, S.-J.; Bao, D.; Shi, M.-M.; Wulan, B.-R.; Yan, J.-M.; Jiang, Q. *Adv. Mater*. **2017**, 29, 1700001.
[14] Bao, D.; Zhang, Q.; Meng, F.-L.; Zhong, H.-X.; Shi, M.-M.; Zhang, Y.; Yan, J.-M.; Jiang, Q.; Zhang, X.-B. *Adv. Mater*. **2017**, 29, 1604799.
[15] Shi, M.-M.; Bao, D.; Wulan, B.-R.; Li, Y.-H.; Zhang, Y.-F.; Yan, J.-M.; Jiang, Q. *Adv. Mater*. **2017**, 29, 1606550.
[16] Song, Y.; Johnson, D.; Peng, R.; Hensley, D. K.; Bonnesen, P. V.; Liang, L.; Huang, J.; Yang, F.; Zhang, F.; Qiao, R.; Baddorf, A. P.; Tschaplinski, T. J.; Engle, N. L.; Hatzell, M. C.; Wu, Z.; Cullen, D. A.; Meyer III, H. M.; Sumpter, B. G.; Rondinon, A. J. A physical catalyst for the electrolysis of nitrogen to ammonia. *Sci. Adv*. **2018**, 4:e1700336
[17] Liu, Y.; Su, Y.; Quan, X.; Fan, X.; Chen, S.; Yu, H.; Zhao, H.; Zhang, Y.; Zhao, J. *ACS Catal*. **2018**, 8, 1186
[18] Trans, K.; Ulissi, Z. W. Active learning across intermetallics to guide discovery of electrocatalysts for CO_2 reduction and H_2 evolution. *Nat. Catal*. **2018**, 1, 696-703
[19] Panapitiya, G.; Avendano-Franco, G.; Ren, P.; Wen, X.; Li, Y.; Lewis, J. P. Machine-learning prediction of CO adsorption in thiolated, Ag-alloyed Au nanoclusters. *J. Am. Chem. Soc*. **2018**
[20] Noh, J.; Back, S.; Kim, J.; Jung, Y. Active learning with non-*ab* initio input features toward efficient CO_2 reduction catalysts. *Chem. Sci.* **2018**, 9, 5152-5159.

[21] Meyer, B.; Sawatlon, B.; Heinen, S.; Lilienfeld, O. A. v.; Corminboeuf, C. Machine learning meets volcano plots: computational discovery of cross-coupling catalysts. *Chem. Sci*. **2018**, 9, 7069
[22] Ma, X.; Li, Z.; Achenie, E. K.; Xin, H. Machine-learning-augmented chemisorption model for CO_2 electroreduction catalyst screening. *J. Phys. Chem. Lett*. **2015**, 6, 3528-3533
[23] Toyao, T.; Suzuki, K.; Kikuchi, S.; Takakusagi, S.; Shimizu, K.-i.; Takigawa, I. Toward effective utilization of methane: machine learning prediction of adsorption energies on metal alloys. *J. Phys. Chem. C* **2018**, 122, 8315-8326
[24] Raymond, G.; Shi, H.; Ramasubramaniam, A. Adsorption of CO on low-energy, low-symmetry Pt nanoparticles: energy decomposition analysis and prediction via machine-learning models. *J. Phys. Chem. C*. **2017**, 121, 5612-5619
[25] Kitchin, J. R. Machine learning in catalysis. *Nat. Catal*. **2018**, 1, 230-232
[26] Jinnouchi, R.; Asahi, R. Predicting catalytic activity of nanoparticles by a DFT-aided machine-learning algorithm. *J. Phys. Chem. Lett*. **2017**, 8, 4279-4283
[27] Ulissi, Z. W.; Medford, A. J.; Bligaard, T.; Norskov, J. K. To address surface reaction network complexity using scaling relations machine learning and DFT calculations. *Nat. Commun*. **2017**, 8:14621
[28] Duvenaud, D.; Maclaurin, D.; Aguilera-Iparraguirre, J.; Gomez-Bombarelli, R.; Hirzel, T.; Aspuru-Guzik, A.; Adams, R. P. Convolutional network on graphs for learning molecular fingerprints. *Proc. Advances in Neural Information Processing Systems.* **2015**, 28, 2224-2232
[29] Schutt, K. T.; Arbabzadah, F.; Chmiela, S.; Muller, K. R.; Tkatchenko, A. Quantum-chemical insights from deep tensor neural network. *Nat. Commun*. **2017**, 8:13890
[30] Xie, T.; Grossman, J. C. Crystal graph convolutional neural network for accurate and interpretable prediction of material properties. *Phys. Rev. Lett*. **2018**, 120, 145301
[31] Ahmad, Z.; Xie, T.; Maheshwari, C.; Grossman, J. C.; Viswanathan, V. Machine learning enabled computational screening of inorganic solid electrolytes for suppression of dendrite formation in lithium metal anodes. *ACS Cent. Sci*. **2018**, 4, 996-1006
[32] Isayev, O.; Oses, C.; Toher, C.; Gossett, E.; Curtarolo, S.; Tropsha, A. Universal fragment descriptor for predicting properties of inorganic crystals. *Nat. Commun*. **2017**, 8:15679
[33] Montoya, J. H.; Tsai, C.; Vojvodic, A.; Norskov, J. K. The challenge of electrochemical ammonia synthesis: a new perspective on the role of nitrogen scaling relations. *ChemSusChem* **2015**, 8, 2180-2186
[34] Skulason, E.; Bligaard, T.; Gudmundsdottir, S.; Studt, F.; Rossmeisl, J.; Abild-Pedersen, F.; Vegge, T.; Jonsson, H.; Norskov, J. K. A theoretical evaluation of possible transition metal electro-catalysts for N_2 reduction. *Phys. Chem. Chem. Phys*. **2012**, 14, 1235-1245
[35] Dynamic Periodic Table. https://ptable.com (accessed on December 7, 2018)
[36] Xie, T.; Grossman, J. C. Hierachical visualization of materials space with graph convolutional neural networks. *J. Chem. Phys*. **2018**, 149, 174111
[37] Kresse, G.; Joubert, D. From Ultrasoft Pseudopotentials to the Projector Augmented-Wave Method. *Phys. Rev. B.* **1999**, 59, 3.
[38] Blochl, P. E. Projector Augmented-Wave Method. *Phys. Rev. B.* **1994**, 50, [40]
[39] Hammer, B.; Hansen, L. B.; Nørskov, J. K. Improved Adsorption Energetics within Density-Functional Theory Using Revised Perdew-Burke-Ernzerhof Functionals. *Phys. Rev. B.* **1999**, 59, 11.

[40] Moellmann, J.; Grimme, S. DFT-D3 Study of Some Molecular Crystals. *J. Phys. Chem. C.* **2014**, 118, 7615-7621
[41] Monkhorst, H. J.; Pack, J. D. Special Points for Brillonin-Zone Integrations. *Phys. Rev. B.* **1976**, 13, 12
[42] Skulason, E. *et al. Phys. Chem. Chem. Phys.* **2012**, 14, 1235.
[43] Montoya, J. H.; Tsai, C.; Vojvodic, A.; Nørskov, J. K. *ChemSusChem* **2015**, 8, 2180.
[44] Clevert, Djork-Arné, Thomas Unterthiner, and Sepp Hochreiter. "Fast and accurate deep network learning by exponential linear units (elus)." *arXiv preprint arXiv:1511.07289* (2015).
[45] Kingma, D. P.; Ba, J. Adam: A method for stochastic optimization. **2014**, *arXiv* preprint *arXiv*:1412.6980
[46] Srivastava, N.; Hinton, G.; Krizhevsky, A.; Sutskever, I.; Salakhutdinov, R. Dropout: a simple way to prevent neural networks from overfitting. *The Journal of Machine Learning Research* **2014**, 15, 1929-1958.

Figures

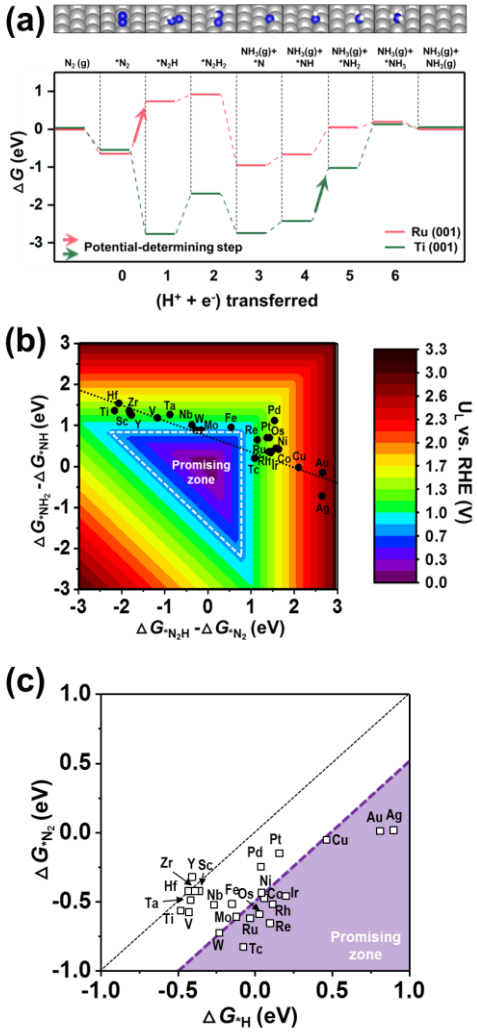

Fig. 1. Adsorption energies as NRR performance descriptors. (a) Free-energy (ΔG) diagrams for associative N_2 reduction pathways on Ru(001) and Ti(001). Corresponding surface/adsorbate structures are shown on top with blue, white, gray atoms represent N, H, Ru (or Ti). (b) 2D Contour plot of limiting potential (U_L) as a function of potential limiting steps with two cases ($^*N_2+H^++e^-\rightarrow {}^*N_2H$ vs. $^*NH+H^++e^- \rightarrow {}^*NH_2$) Calculation results of 24 transition metals (close-packed surface) are added on the map. (c) Comparison of the free energies of N_2 and H adsorbates for 24 transiton metals. Promising zones in both (b) and (c) are referenced to Mo(110).

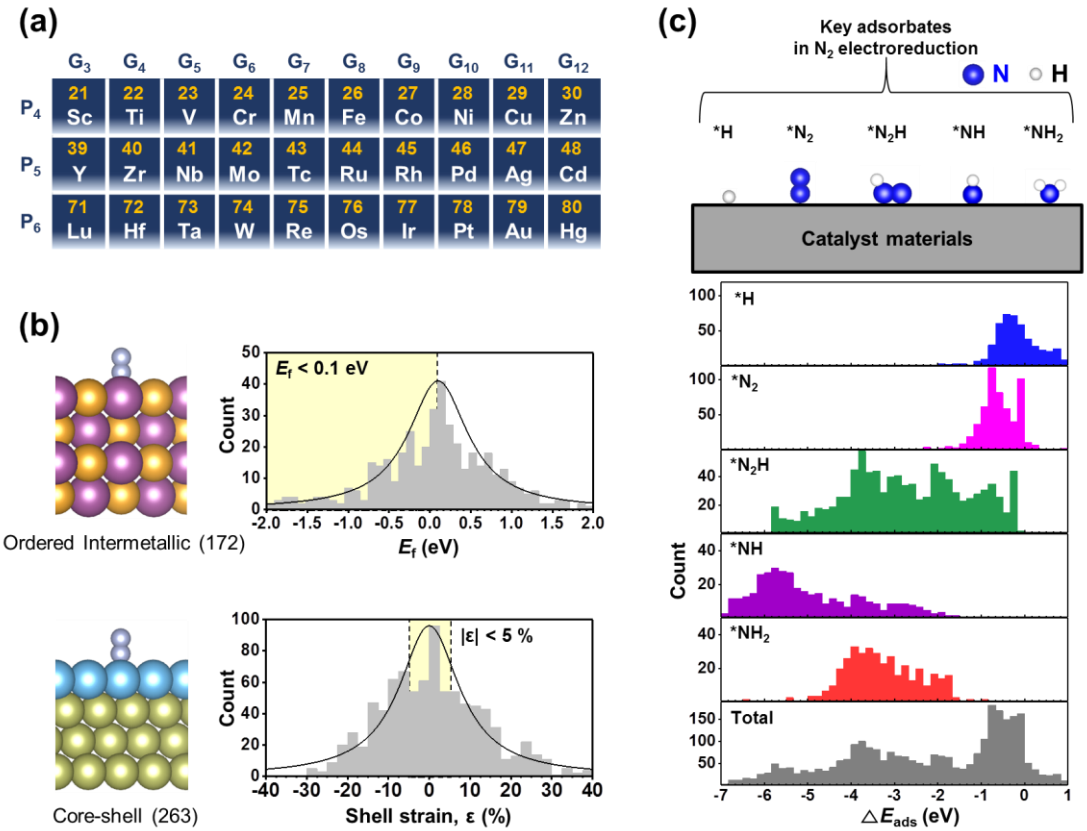

Fig. 2. Database generation. (a) A part of Periodic-Table-of-Elements (group numbers 3-12, and period numbers 4-6). (b) Two types (201 OI systems and CS 263 systems) are considered for catalyst materials. An exemplary structure and distributions (over E_f for OI or ε for CS type) are shown. For both, samples in the yellow shade are selected for surface DFT calculations. (c) A schematic of catalytic system with five key adsorbates in NRR (Upper). Binding energy populations ($\Delta E_{ads.}$) are shown for each adsorbate and total (Lower).

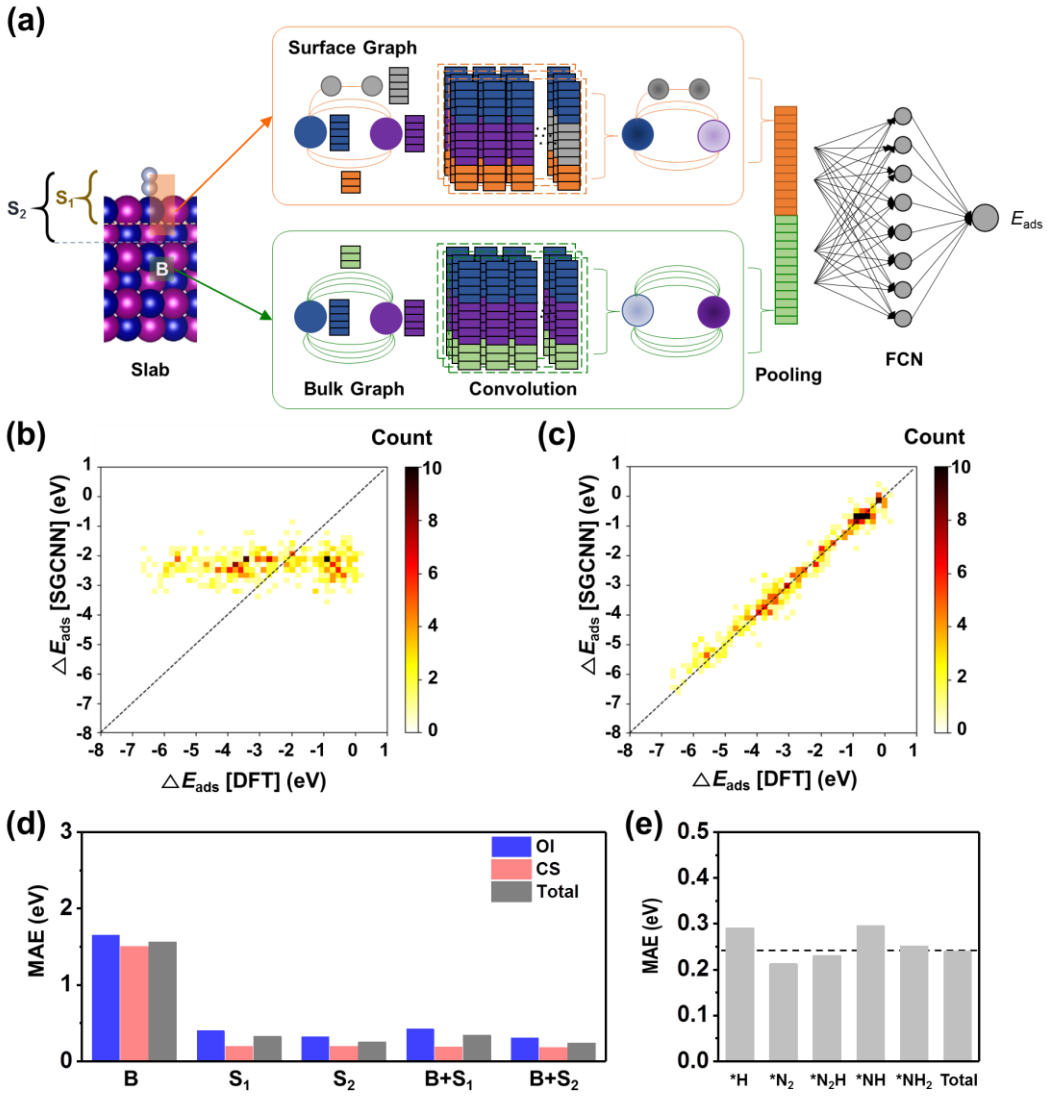

Fig. 3. SGCNN performance. (a) A SGCNN scheme. Each B and S_1 (or S_2) represents bulk graph and surface graph with top one (or two) layers. Details of convolution/pooling/activation functions, and network structures are available in the Method section. (b-c) 2D histogram comparing the predicted adsorption energies by SGCNN model and DFT computation. (b) is the case when only bulk graph (B) is used. (c) is the case when both B and S_2 are simultaneously used (B+S_2). (d) Comparison of MAE values for 5 different graph structures (B, S_1, S_2, B+S_1, and B+S_2). (e) Comparison of MAE values for H, N_2, N_2H, NH, and NH_2 adsorbates, with the dashed line indicating MAE of total.

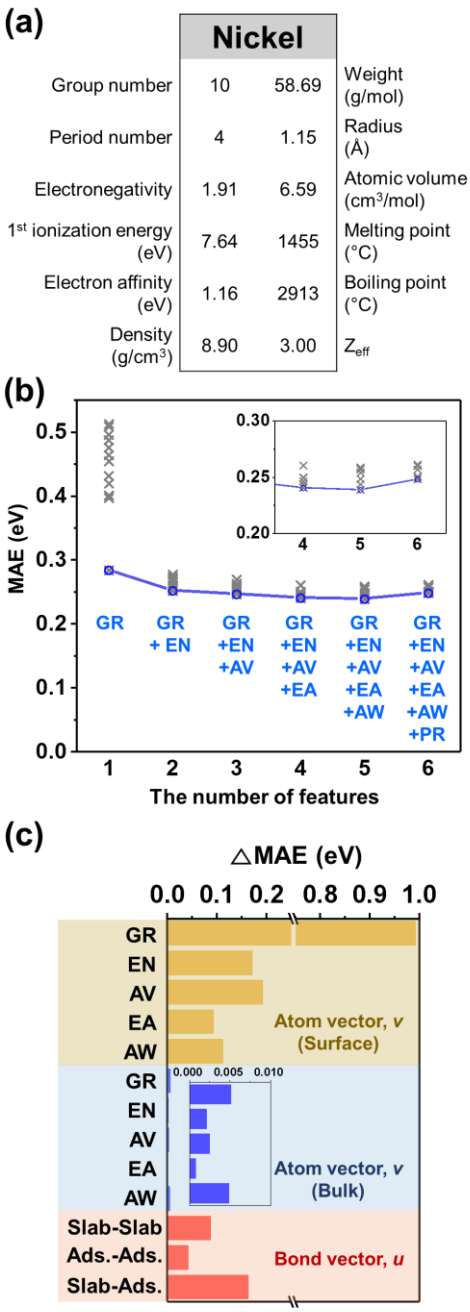

Fig 4. Input features of the SGCNN model. (a) Types of atomic input features (12 elemental properties for Ni element, as an example) tested for SGCNN training. (b) Feature optimization tests. MAE values as a function of various feature combinations. Blue points/line denote the minimum value at each feature number. (GR, EN, AV, EA, AW) combination is the best, leading to minimum MAE of 0.23 eV. (c) Feature occlusion sensitivity test. The increase of MAE (ΔMAE) is shown when a specific feature of atom or bond vector is occluded with all zero entries.

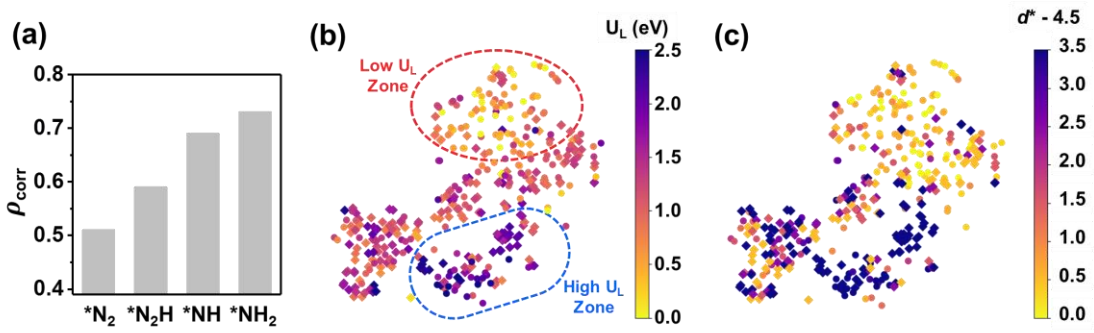

Fig 5. *t*-SNE analysis. (a) Pearson correlation between U_L and adsorption energy of each adsorbate ($^*N_2$, $^*N_2H$, $^*NH$, $^*NH_2$). (b) *t*-SNE analysis of feature vectors of NH_2 adsorbate cases with the colour of U_L. *x* and *y* axes here are a reduced 2D feature space. Low UL and high UL zones are highlighted. Top candidates with lowest UL values are also highlighted. (c) *t*-SNE of the same feature vector with the coulor of d^*-4.5. d^* is defined as the averaged *d*-electron occupation of top surface layer: $d^*=(d_A+d_B)/2$ for OI, and d_{Shell} for CS where d_X is *d*-block electron number of X element.

Supporting Information for

Slab Graph Convolutional Neural Network for Discovery of N_2 Electroreduction Catalysts

Myungjoon Kim[+], Byung Chul Yeo[+], Sang Soo Han[*], Donghun Kim[*]

Computational Science Research Center, Korea Institute of Science and Technology, Seoul 02792, Republic of Korea

[*]Correspondence to: donghun@kist.re.kr (D.K.); sangsoo@kist.re.kr (S.S.H.)
[+]Equal contributions

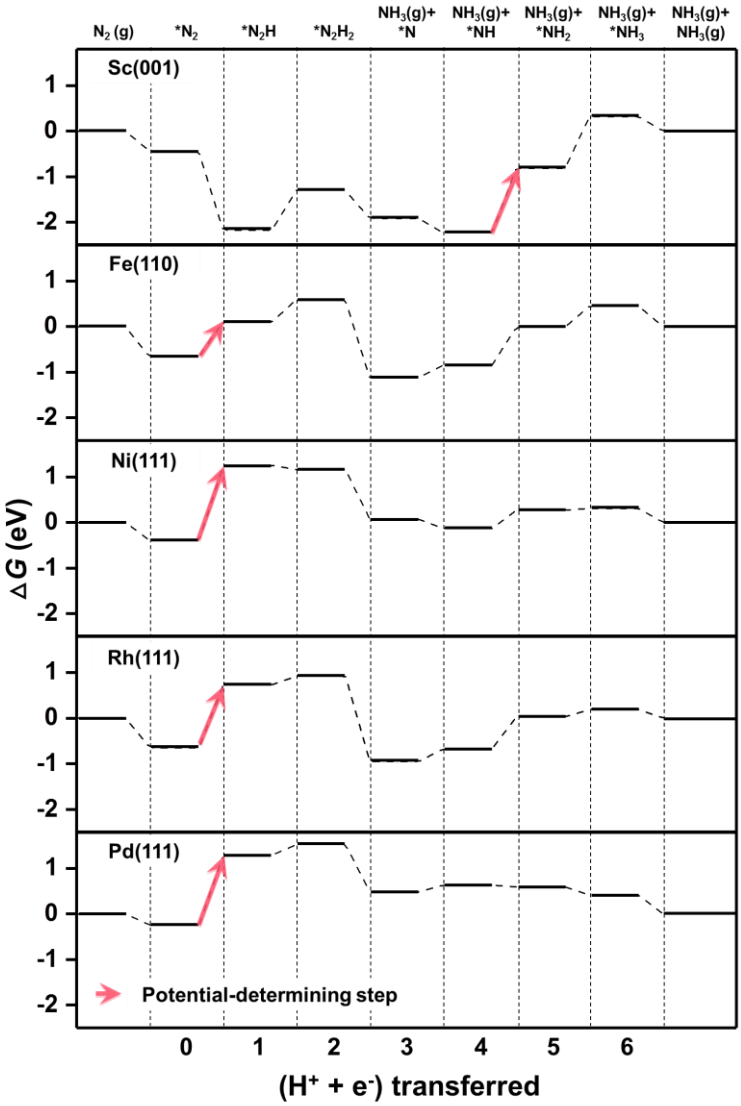

FIG. S1. Free-energy (ΔG) diagrams for associative N_2 reduction pathways on Sc(001), Fe(110), Ni(111), Rh(111), and Pd(001).

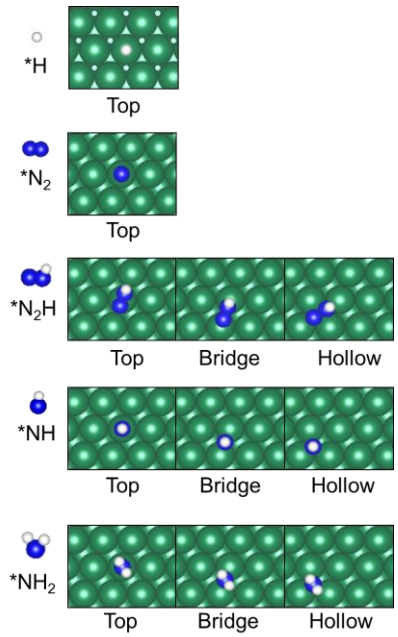

FIG. S2. Various configurations of five adsorbates (*H, *N_2, *N_2H, *NH, and *NH_2) on the catalytic surfaces.

TABLE S1. The zero-point energy correction (ΔG_{ZPE}), enthalpy correction (ΔH_{corr}), entropy correction ($-T\Delta S_{corr}$), and free energy correction (ΔG_{corr}) of five adsorbates for five adsorbates (*H, *N_2, *N_2H, *NH, and *NH_2). All values are given in eV. The free energy correction is estimated by the following equation:
$\Delta G_{corr} = \Delta G_{ZPE} + \Delta H_{corr} - T\Delta S_{corr}$.

Adsorbates	ΔG_{ZPE}	ΔH_{corr}	$-T\Delta S_{corr}$	ΔG_{corr}
*H	0.16	0.01	-0.01	0.16
*N_2H	0.48	0.07	-0.13	0.42
*NH	0.38	0.03	-0.04	0.37
*NH_2	0.69	0.05	-0.08	0.66
*N_2	0.20	0.09	-0.18	0.11

Table S2. Performance comparison between our model and previous reported machine learning models

Ref.	Algorithm	Input features	Adsorbate /Slab	Prediction accuracy			
				RMSE (eV)	MAE (eV)	n-RMSE	n-MAE
SGCNN (present work)	Graph-CNN	Atomic features, readily available from periodic table (group, period, radius, EN, IE, EA, melting point)	N_2, N_2H, NH, NH_2 /Metal alloy	0.35	0.23	0.044	0.029
[1]	LASSO+l_0	- Oxide formation energy - O-vacancy formation energy	Single metal atom /Oxide	0.91	N/A	0.057	N/A
[2]	KRR	- *d*-band width - Electronegativity	CO /Metal alloy-(100)	N/A	0.05	N/A	0.025
[3]	GBR	- *d*-band center - Coordination number - Adsorption energy	CO /Pt	N/A	0.12	N/A	0.06
[4]	ANN	- *d*-band filling, center, width, skewness, kurtosis - Pauling electronegativity	CO /Metal alloy	0.12	N/A	0.063	N/A

Terminology abbreviations. CNN=convolutional neural network; LASSO=least absolute shrinkage and selection operator; KRR=kernel ridge regression; GBR=gradient boosting regression; ANN=artificial neural network; EN=electronegativity; IE=1st ionization energy; EA=electron affinity; n-RMSE=normalized RMSE, or RMSE/(E_{max}-E_{min}); n-MAE=normalized MAE, or MAE/(E_{max}-E_{min}).

References

[1] N. J. O'Connor, A. S. M. Jonayat, M. J. Janik, and T. P. Senftle, *Nat. Catal.* 1, 531-539 (2018)

[2] J. Noh, S. Back, J. Kim, Y. Jung, *Chem. Sci.* 9, 5152 (2018)

[3] R. Gasper, H. Shi, A. Ramasubramaniam, *J. Phys. Chem. C* 121, 5612 (2017)

[4] X. Ma, Z. Li, L. E. K. Achenie, H. Xin, *J. Phys. Chem. Lett.* 6, 3528 (2015)

Table S3. A list of hyperparameters and their ranges for optimization process.

Hyperparameter	Range
Number of convolutional layers	1, 2, 3, 4
Number of convolutional filters	1, 2, 3
Number of fully-connected layers	1, 2, 3
Number of neurons	2, 10, 20
Learning rate	10^{-5}, 10^{-4}, 10^{-3}, 10^{-2}, 10^{-1}
Decaying learning rate (for every 100 step)	0.90, 0.95, 0.98, 0.99
L^2 regularization coefficient	10^{-3}, 10^{-2}, 10^{-1}
Dropout probability	0.5, 0.6, 0.7, 0.8, 0.9
Batch size	32, 64, 128, 256
Epochs	300, 500, 800, 1000
Standard deviation of initial weights	10^{-3}, 10^{-2}, 10^{-1}

Table S4. A list of hyperparameters and their ranges for optimization process.

Input feature used in atom vectors	Range	Unit	Category #
Group number	1, 3 – 12, 15		12
Period number	1 – 5		5
Electronegativity	1.2 – 3.2		10
1st ionization energy	6.5 – 15	eV	10
Electron affinity	-0.8 – 2.4	eV	10
Density	0 – 23	g/cm^3	10
Weight	1 – 240	g/mol	10
Radius	0 – 1.65	Å	10
Atomic volume	6.5 – 18	cm^3/mol	10
Melting point	-260 – 3500	℃	10
Boiling point	-274 – 5600	℃	10
Z_{eff}	1 – 5.3		10

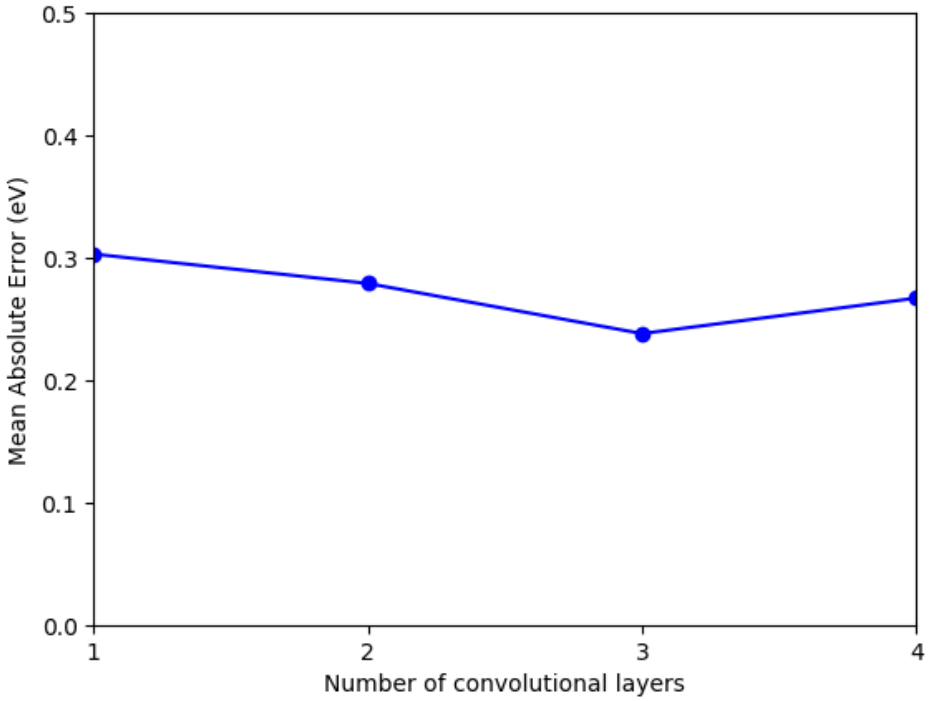

FIG. S3. The effect of the number of convolutional layers